RESEARCH

ENVINet5 deep learning change detection framework for the estimation of agriculture variations during 2012–2023 with Landsat series data

Gurwinder Singh [ID] · Neelam Dahiya [ID] ·
Vishakha Sood [ID] · Sartajvir Singh [ID] ·
Apoorva Sharma [ID]

Abstract Remote sensing is one of the most important methods for analysing the multitemporal changes over a certain period. As a cost-effective way, remote sensing allows the long-term analysis of agricultural land by collecting satellite imagery from different satellite missions. Landsat is one of the longest-running world missions which offers a moderate-resolution earth observation dataset. Land surface mapping and monitoring are generally performed by incorporating classification and change detection models. In this work, a deep learning-based change detection (DCD) algorithm has been proposed to detect long-term agricultural changes using the Landsat series datasets (i.e., Landsat-7, Landsat-8, and Landsat-9) during the period 2012 to 2023. The proposed algorithm extracts the features from satellite data according to their spectral and geographic characteristics and identifies seasonal variability. The DCD integrates the deep learning-based (Environment for visualizing images) ENVI Net-5 classification model and posterior probability-based post-classification comparison-based change detection model (PCD). The DCD is capable of providing seasonal variations accurately with distinct Landsat series dataset and promises to use higher resolution dataset with accurate results. The experimental result concludes that vegetation has decreased from 2012 to 2023, while build-up land has increased up to 88.22% (2012–2023) for Landsat-7 and Landsat-8 datasets. On the other side, degraded area includes water (3.20–0.05%) and fallow land (1–0.59%). This study allows the identification of crop growth, crop yield prediction, precision farming, and crop mapping.

Keywords Agriculture · Classification · Change detection · Algorithm · Remote sensing

G. Singh
School of Sciences, Noida International University,
Sector-17A, Noida, Uttar Pradesh 203201, India
e-mail: gurwindersingh.balahara@gmail.com

N. Dahiya
Chitkara University Institute of Engineering
and Technology, Chitkara University, Chandigarh,
Punjab 140401, India
e-mail: neelam.rani@chitkara.edu.in

V. Sood
Department of Civil Engineering, Indian Institute
of Technology, Ropar 140001, India
e-mail: vishakha.sood@ieee.org

S. Singh (✉) · A. Sharma
Department of Computer and Engineering, University
Institute of Engineering, Chandigarh University,
Chandigarh, Punjab 140413, India
e-mail: sartajvir.dhillon@gmail.com

A. Sharma
e-mail: er.apoorva.sharma@gmail.com

Introduction

Remote sensing is one of the most important methods for analysing the multitemporal changes over a

certain period. The land surface observation is important for efficient management of natural resources like water, soil, and vegetation and the climate impact on these resources. However, the degradation of land is considered an important factor affecting sustainable agriculture and continuous monitoring globally is essential for food security (Alshari et al., 2023). The primary causes of this deterioration might be severe natural disasters like floods and landslides, as well as other man-made causes. Thus, timely and accurate information on changes in land cover can assist a variety of undesirable surface changes that might otherwise result in a shortage of natural resources (Jozdani et al., 2019; Twisa & Buchroithner, 2019). Traditionally, land cover change monitoring has been done using on-the-ground observations which is time-consuming (Eugene et al., 2022; Mountrakis & Heydari, 2023). On the other hand, remote sensing is a powerful tool that plays an important role in monitoring, depicting, and managing regular changes with the help of information captured through satellite imagery (Gusain et al., 2019; Taloor et al. 2020). It is useful in many fields, including agriculture, forest monitoring, and weather forecasting. Two methods, namely categorization and change detection, are widely employed to extract vital and precise information regarding changes in the earth's surface (Mahmoud et al., 2023; Pande, 2022).

Classification simplifies the data for users to analyse spatial patterns and correlations by classifying the pixels into several categories such as water, agriculture, and urban. During the past decade, various classifiers based on machine and deep learning have been developed for land cover changes (Teluguntla et al., 2018; C. Zhang et al., 2019). In past studies, classification algorithms such as random forest classifier (RF) (Alshari et al., 2023; Zerrouki et al., 2019), artificial neural network classifier (ANN) (e Silva et al., 2020; Zerrouki et al., 2019), the k-nearest neighbour classifier (KNN) (Zerrouki et al., 2019), and support vector machine classifier (SVM) (Shao & Lunetta, 2012) have been tested for different applications using multispectral/optical remote sensing data (Singh et al., 2021d; Singh e al., 2022c). Some researchers also developed and improved deep learning-based classifiers such as deep neural network classifier (DNN) (Al-Dousari et al., 2023; Bali & Singla, 2021; Liang et al., 2022), recurrent neural network classifier (RNN) (Chen et al., 2019;

Henry et al., 2019), and convolutional neural network classifier (CNN) (S. Kaur et al., 2022; Yao et al., 2020) to improve accuracy, processing speed and applicability.

Different change detection strategies have been used by numerous researchers to report their work on land use and land-cover (LULC) (Lu et al., 2004; 2014). Some change detection methods, including image differencing with a multispectral dataset, are suggested and contrasted with the decision tree algorithm using the PCC methodology (Dahiya et al., 2023). Goswami et al. (2022) represented the machine learning-based change detection method for the estimation of LULC variations. Similarly, Y. Zhang et al. (2022) suggested a continuous change detection approach to track changes in the forest across China by employing an index method and a multispectral dataset. Three categories in total—forest, water, and others—are employed, and the modified map's accuracy of 86.4% was attained. As a result, the effectiveness of various classifiers depends on the category of classification dataset that is being used. Additionally, the results of the classification process will directly influence the accuracy of subsequent processing like change detection (Boonpook et al., 2023; Zamani et al., 2022). Deep learning is one of the effective approach to resolve the various challenging issues in the processing of the datasets but on the other hand offers the automated training process, less dependent on human interface, improved performance in intricate scenarios, and the absence of stringent requirements for verifying the quality of training data (Felegari et al., 2023; L. Zhang et al., 2016). Figure 1 briefly summarizes the processing of various deep learning models.

Change detection is a process of measuring the multitemporal changes with respect to the object or particular region by observing it at distinct times (Basheer et al., 2022; A. Singh, 1989). Deep learning has proven an effective approach in the change detection technique due to its numerous benefits, therefore deep learning-based changed detection (DCD) concept has been explored in this study. It is capable of providing seasonal variations accurately with distinct Landsat series dataset and promise to use higher resolution dataset with accurate results. Practically, it helps in recognizing the differences or variations between multitemporal satellite images. Change detection technique serves various application areas such as forest fire, tracking cyclones, deforestation, and urban
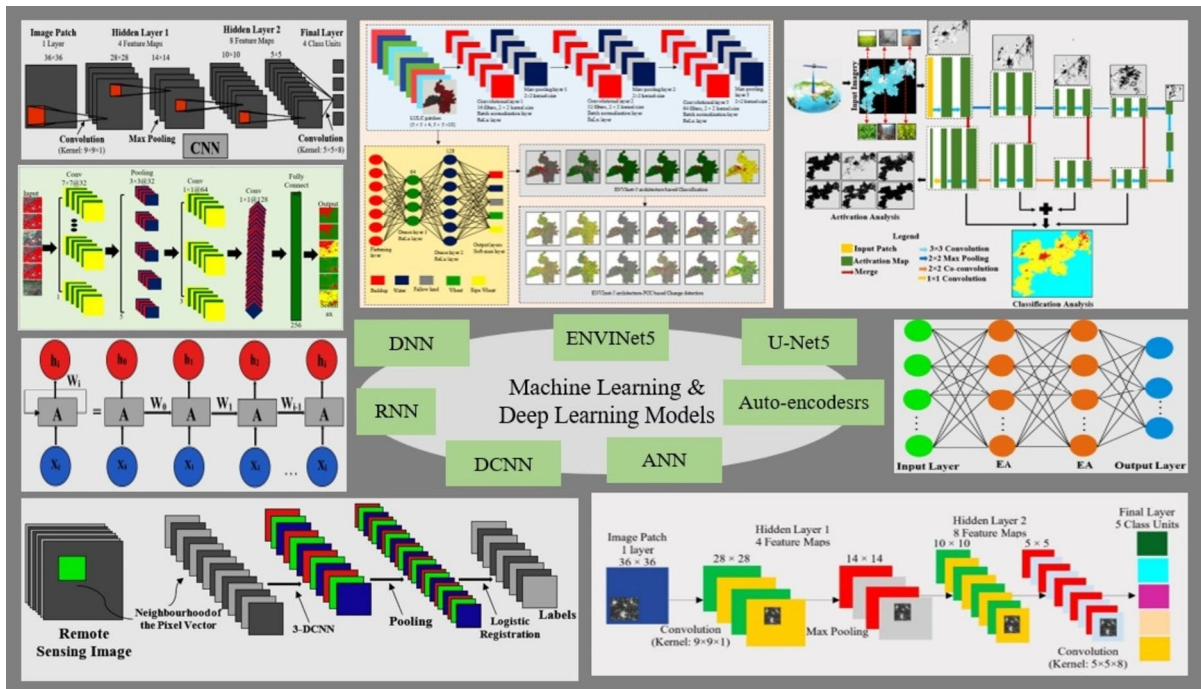
Fig. 1 Brief overview of various deep learning models

evolution (Sing et al., 2022a). In previous literature, various change detection methods have emerged which can be further broadly classified into per-pixel and sub-pixel (Esmaeili et al., 2023). Per-pixel means a single pixel belongs to one category of class whereas, sub-pixel means that a single pixel in an image can belong to multiple memberships of multiple class categories. There are various per-pixel-based methods namely image rationing (IR), post-classification comparison (PCC), change vector analysis (CVA), and image differencing (ID) (Farmonov et al., 2023). The choice of change detection technique depends upon the type of earth features under observation. The identification of various land surface changes may be accomplished through change detection techniques. While implementing the change detection, the four criteria must be fulfilled i.e., (a) explicit multi-temporal dataset registration; (b) accurate radiometric and atmospheric evaluation; (c) comparable phenological states between different datasets; and (d) the selection of datasets with the same spatial and spectral resolution (Dibs et al., 2023; Kumar et al., 2022;). Table 1 also represents the various machine learning and deep learning techniques for agricultural land as shown below.

To effectively monitor land use and record land change resulting from a variety of natural and human-caused changes, including urbanization, drought and climate change, Landsat satellites are equipped with the best ground resolution and spectral bands for agriculture purpose. R. K. Singh, Sethi, and Singh (2021a) uses machine learning algorithm for LULC detection using Landsat series dataset and achieved accuracy below 86%. Similarly, Y. Zhang et al. (2022) suggested a continuous change detection strategy to monitor the forest utilizing a multispectral dataset using an index method over the country of China with three categories and achieved accuracy of 86.4%. To improve the results and to fetch detailed information about LULC, deep learning-based approach is used. It promises to employ better resolution datasets with reliable findings and is capable of presenting seasonal changes using various Landsat series datasets.

The present article aims to evaluate the performance of deep learning-based ENVINet-5 architecture for agriculture using Landsat time series data, i.e., Landsat-7, Landsat-8, and Landsat-9. Therefore, the objectives are framed as follow: (a) implementation of the deep learning-based ENVINet-5 architecture using

Table 1 Agricultural land with machine learning and deep learning techniques

Category	Classifier	Sensor	Crop/Parameter	Performance	Reference
Machine Learning	[1]RVM	Sentinel-1	Flood mapping	89%	(Sharifi, 2020)
Machine Learning	[2]ALOS, [3]DEM	Sentinel-2	Flood mapping	-	(Tariq et al., 2022)
Fuzzy Logic	[4]WLC	Landsat-8	Slope for surface, Soil texture, Irrigation capability	-	(Zamani et al., 2022)
Machine Learning	[5]CNN, [6]RF	Hyperspectral	Corn, Soybean, Sunflower, Wheat	96.48%	(Farmonov et al., 2023)
Pixel-based, Object-based	[5]CNN, [1]RVM, [6]RF, [7]SVM, [8]BT, [9]SAE	Satellite	River, Tree, Shadow, Road, Building, Green space	93.8%	(Mohammadi & Sharifi, 2021)
Machine Learning	[5]CNN	MODIS	Crop yield prediction	-	(Nejad et al., 2023)
Machine Learning	[5]CNN, [10]ICD	Landsat-5, Landsat-7, Landsat-8	Agriculture, Water, Oak Forest, mixed forest, Barre land, Rangeland	-	(Moradi & Sharifi, 2023)
Deep Learning	[5]CNN	Sentinel-2	Vegetation, Buildup, Water, Mix-Buildup, Mix-Water & Vegetation	80%	(G. Singh et al., 2021b)
Machine Learning	[11]ANN, [12]NNF, [13]PCC	MODIS, SCATSAT-1	Crop yield prediction	91.8%	(R. Kaur et al., 2023)
Machine Learning, Deep Learning	[5]CNN, [6]RF, [7]SVM, [114]DLCD, [13]PCC	Sentinel-2	Vegetation, Buildup, Water, Fallow land, Ripe	97.2%	(G. Singh, Singh, et al., 2022a)

[1]RVM relevance vector machine, [2]ALOS advanced land observation satellite, [3]DEM digital elevation model, [4]WLC weighted linear combination method, [5]CNN convolutional neural network, [6]RF Random Forest, [7]SVM support vector machine, [8]BT bagging trees, [9]SAE sparse auto-encoder, [10]ICD image change difference, [11]ANN artificial neural network, [12]NNF nearest-neighbour-based image fusion, [12]PCC post-classification comparison, [14]DLCD deep learning-based change detection.

the Landsat time series dataset, (b) development of the DCD model, and (c) accuracy assessment of the DCD model using the Landsat time series dataset. The outcome of this study allows the efficient estimation of agricultural changes with a state-of-the-art ENVINet-5-based deep learning change detection model. This introduction section is followed by the study area and satellite dataset. Afterwards, the methodology and experimental results have been discussed. At last, the conclusion has been drawn based on the results and discussion.

Study area and satellite dataset

Study area

The District Fatehgarh Sahib, situated in the southeastern region of Punjab (India) is selected for the study purpose as shown in Fig. 2. This region

has geographic coordinates between 30°38′44″ N to 30°38′37″ N in latitude and 76°22′57″ E to 76°22′95″ E in longitude. It is one of the developed districts of Punjab having a geographic area of 1147 km². It is an agrarian region and most of the area lies in fertile alluvial soil which is good for agricultural cultivation. The Fatehgarh Sahib District's residents primarily depend on agriculture for their livelihood. It contains a net irrigated area of about 101,000 hectares, whereas the gross irrigated area is 191,000 hectares. The land use and land cover-based classes that are selected for this region include wheat, ripe wheat, fallow land, buildup area, and water. Therefore, deep analysis is required to understand the special effects of human activity on the ecosystem and create plans for sustainable land use and management. As of now, the cost-effective method of monitoring and mapping land cover changes and other agricultural areas is only provided by remote sensing.

Fig. 2 Representation of study area (**a**) Indian map highlights the Punjab state, (**b**) Punjab map highlights the district Fatehgarh Sahib, and (**c**) the district Fatehgarh Sahib dataset Landsat (RGB: NIR-Red-Green) bands based natural color images.
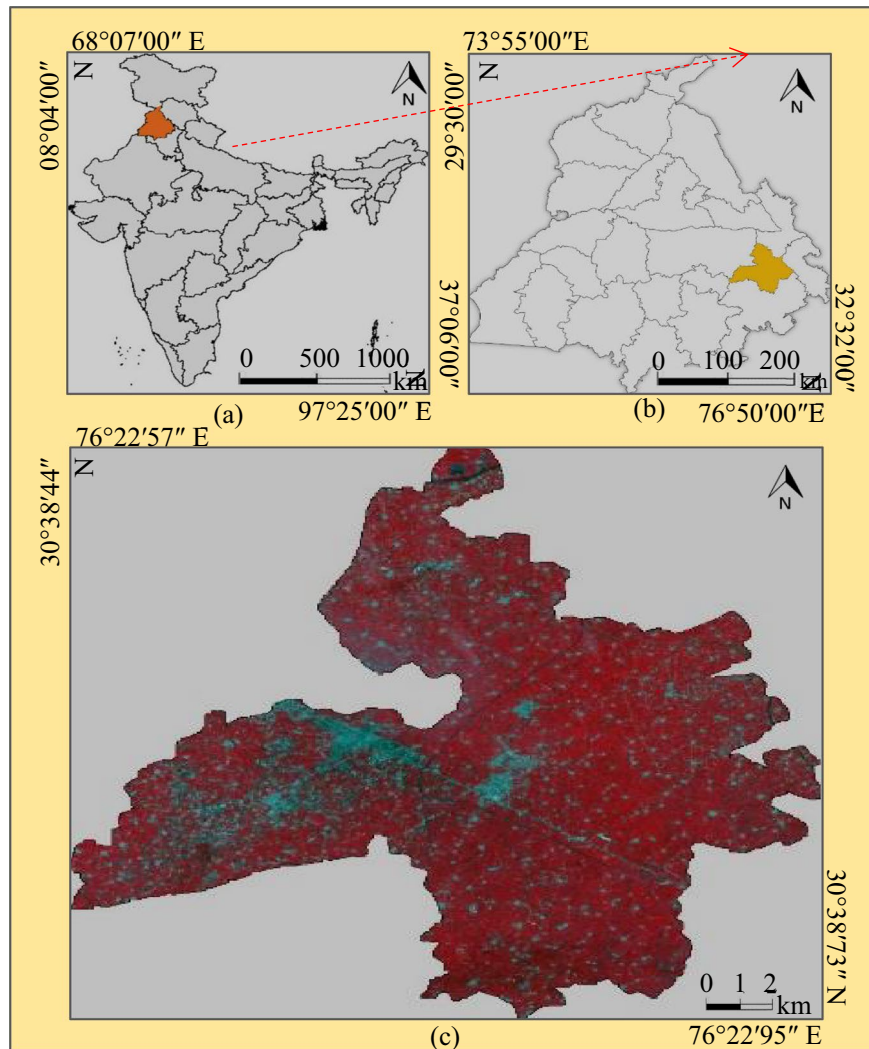
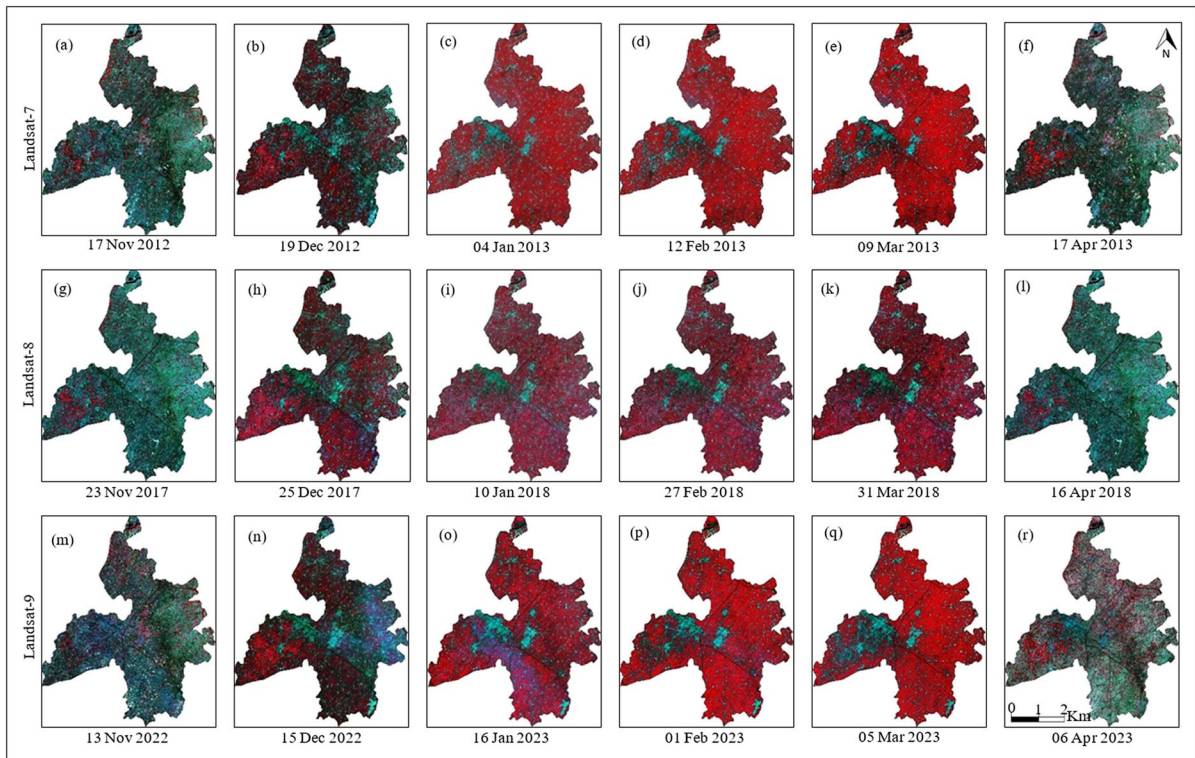## Dataset

The multispectral cloud-free datasets namely Landsat-7, Landsat-8, and Landsat-9 have been used for the present research work as shown in Fig. 3. The Landsat-7 dataset was acquired from Nov-2012 to April-2013. The dataset acquisition dates are: (a) 17-Nov-2012, (b) 19-Dec-2012, (c) 04-Jan-2013, (d) 12-Feb-2013, (e) 09-Mar-2013, and (f) 17-Apr-2013. Landsat 8 dataset was acquired from Nov-2017 to April-2018 and the dataset acquisition dates are: (a) 23-Nov-2017, (b) 25-Dec 2017, (c) 10-Jan-2018, (d) 27-Feb-2018, (e) 31-Mar-2018, and (f) 16-Apr-2018. Landsat-9 dataset was acquired from Nov-2022 to April-2023 and the dataset acquisition dates are (a) 13-Nov-2022, (b) 15-Dec-2022, (c) 16-Jan-2023, (d) 01-Feb-2023, (e) 05-Mar-2023, and (f) 06-Apr-2023. As per the availability and to notice the seasonal variations at different time intervals, data from three different sources are used, but the same bands are used for all the datasets.

The Landsat-7 dataset has dimensions of 4.04 m × 2.74 m and weights 1973 kg. There are 378 Gbits (around 100 pictures) of solid-state memory on board Landsat-7. The primary equipment on board Landsat-7 is the image sensor known as the Enhanced Thematic Mapper Plus (ETM+), which is a whisk broom scanner. On February 11, 2013, Landsat 8 was launched on an Atlas-V 401 rocket from Vandenberg Air Force Base in California, using an extended payload fairing (EPF) provided by United Launch Alliance, LLC. The Thermal

Fig. 3 Landsat-7 datasets (NIR-Red-Green) acquired on November 2012 to April 2013 (**a–f**), Landsat-8 datasets (NIR-Red-Green) acquired on November 2017 to April 2018 (**g-l**), and Landsat-9 datasets (NIR-Red-Green) acquired on November 2022 to April 2023 (**m–r**)

Infrared Sensor (TIRS) and the Operational Land Imager (OLI) are the two scientific instruments that make up the Landsat 8 satellite payload. Seasonal coverage of the whole landmass is offered by these two sensors at three different spatial resolutions: 30 m for visible, NIR, and SWIR; 100 m for thermal; and 15 m for panchromatic.

On September 27, 2021, Landsat-9 was launched from Vandenberg Air Force Base in California using an Atlas V 401 rocket from United Launch Alliance. The Thermal Infrared Sensor 2 (TIRS-2) and Operational Land Imager 2 (OLI-2) are on board Landsat-9, which was constructed by the NASA Goddard Space Flight Center in Greenbelt, Maryland, and Ball Aerospace & Technologies Corporation in Boulder, Colorado, respectively. The two instruments were integrated and the spacecraft was conceived and built by Northrop Grumman. Landsat-9 can distinguish 16,384 distinct wavelength color. In contrast, 8-bit radiometric resolution of Landsat-7 allows it to distinguish just 256, whereas Landsat

8's 12-bit data allows it to detect 4096 shades. The Landsat series dataset (i.e., Landsat-7, Landsat-8, and Landsat-9) was downloaded from the online portal (https://earthexplorer.usgs.gov/). The Landsat dataset series products offer a temporal resolution of 16 days with a swath width of 185 km. The Landsat 7 has an 8-bit radiometric resolution, whereas, Landsat 8 and 9, it is 12-bit.

During the training and validation phases, Pléiades constellation fine-resolution data, i.e., Pléiades 1A and 1B were applied. Center National d'Etudes Spatiales (CNES), a division of Airbus Defense and Space, oversees this spacecraft. It provides sharp resolution images, which might give more specific information about the area. ERDAS Imagine Earth Resources Data Analysis System (2015) contains an in-built google earth (GE) viewer where a picture may be grounded about the GE. It provides the capacity to link to GE, navigate to a designated place, match images to GE and vice versa and carry out a great deal of recognition and identification

finding the remote sensing equipment. The Pléiades system gives data that may be verified using very high-resolution remote sensing. The distance between tiny things, such as buildings and country roads, may be measured using it. It is also used to provide information to detect and identify crop diseases, differentiate between agricultural and plain land.

Methodology

The framework of the proposed methodology is shown in Fig. 4 which includes (a) the pre-processing of the input image (Landsat series dataset), (b) the implementation of the classification model (ENVI-Net-5), (c) the implementation of change detection technique (DCD), and (d) accuracy assessment.
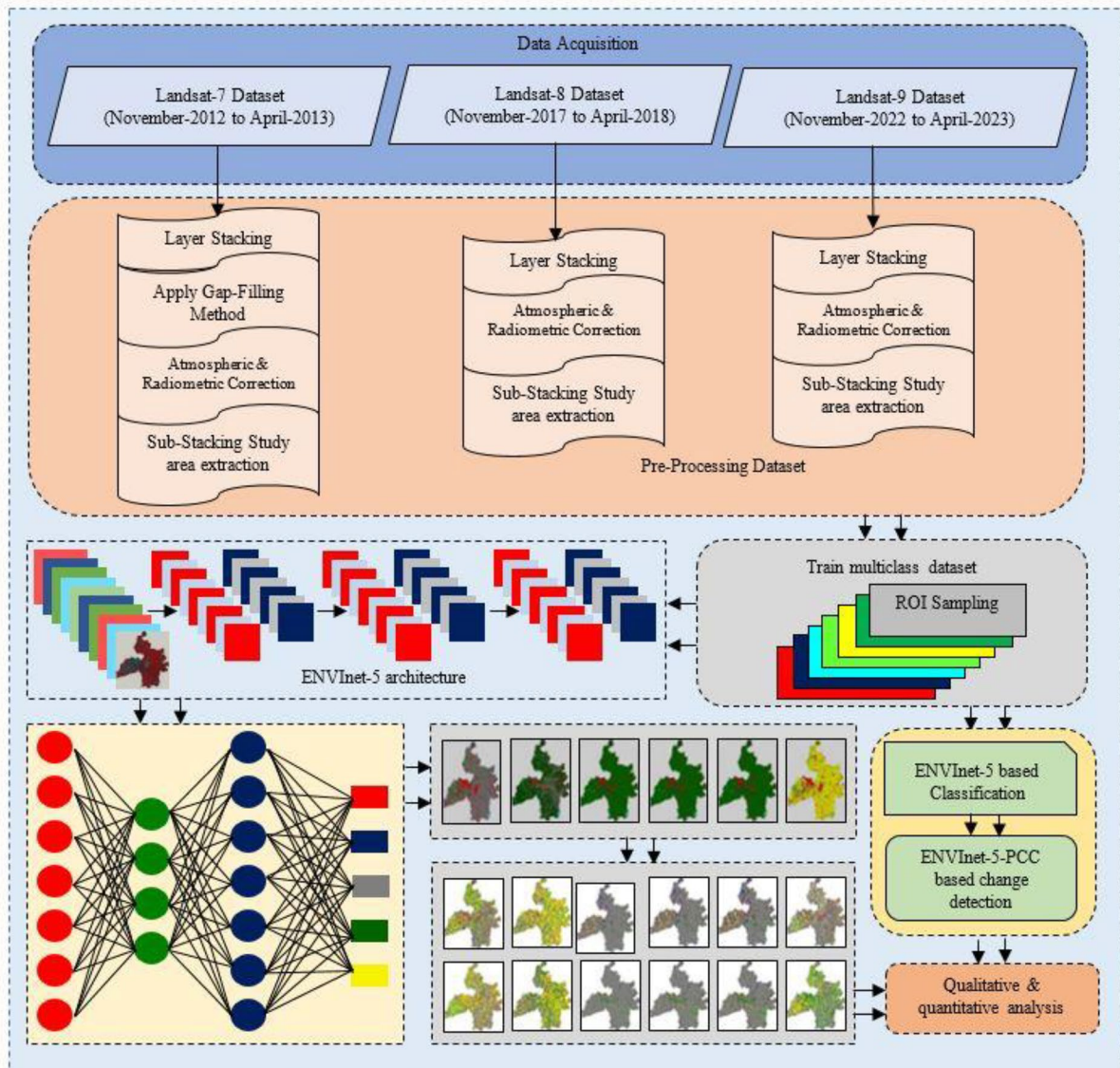
Fig. 4 The framework of ENVINet-5 architecture-based methodology

Preprocessing of an input dataset

The satellite dataset must be pre-processed before applying classification and change detection techniques. It is helpful in the successful elimination of the countless inaccuracies brought by several factors, such as the sun's position in relation to the landscape, the air's fluctuating conditions, and errors created by satellite sensors (Jalayer et al., 2023; Nejad et al., 2023). The outcome might change if the errors are not fixed on time. The radiometric correction, which the sensor uses to store the intensity of electromagnetic radiation (EMR) using digital numbers (DN), is eliminated as part of the pre-processing (Kumar & Jain, 2020; Panahi, Khosravi, et al., 2022; Sharifi & Felegari, 2022).

It is necessary to convert these DN into practical units such as reflectance, radiance, etc. The estimation of reflectance includes the conversion of DN data into radiance values. The brightness value of the DN imagery may be calculated by taking into account the maximum and minimum radiance values of each band (Gusain et al., 2019). The value of Xi as radian is computed as shown in Eq. (1).

$$x_{i\lambda} = \left[\frac{(DM_i\lambda)}{(Mgray)} \times \left(Bmax_\lambda - Bmin_\lambda\right) \right] + Bmin_\lambda \tag{1}$$

where Bmax is represented as the maximum radiance indicated by the metadata. Bmin is shown as the minimal radiance value, and DMi highlights the digital number of band pixels. The maximum DN value for a given band is represented by MGray. It is important to calculate all the angles, including the solar zenith angle, azimuth angle, and elevation angle. The solar zenith angle, which is the distance between the Sun and its overhead position, is expressed in degrees. Every sensor's readings contain some amount of noise or inaccuracy. While some of this noise can be eliminated, it is not always viable to do so using radiometric corrections. To eliminate or reduce these effects, radiometric adjustments use atmospheric correction algorithms, which enable precise surface property interpretation. In the present study, spectral reflectance is obtained by using Eq. (2) (Mishra et al., 2010) given below.

$$R = D^2 \left(L_r - L_p\right) \pi / t_2 \left(E_0 \cos \theta_z t_z + E_t\right) \tag{2}$$

where L_r and L_p represent the radiance of a sensor, zenith angle is denoted by θ_z, D is used to represent the distance among earth and the sun. E_0 and Et show the bandpass spectral irradiance. After necessary rectification, the image can be used for additional analysis, such as classification or change detection. The accuracy evaluation process is used to validate the findings produced after implementation. Firstly, layer stacking of the Landsat series dataset is done, which means that all desired bands are stacked together to form a single image. After that, the radiometric corrections are performed on the dataset to remove any form of distortion. However, the Landsat-7 dataset suffers from data gap issues due to the scan line corrector (SLC) failing. These gaps are filled with the help of the direct sampling technique (Ienco et al., 2017; Panahi, Yariyan, et al., 2022). After this, corrective measures are applied to the Landsat 7 dataset.

ENVINet-5 architecture-based classification model

Classification allows the identification or analysis of objects to categorize them into specific sets of classes with the help of a training dataset. Numerous categorization techniques have been developed for land cover mapping in earlier literature. However, past literature assured that deep learning classifiers performed better than machine learning classifiers due to numerous benefits such as being capable of dealing with complex data, rapid model development, and minimal user involvement. In this study, we have proposed a deep learning-based ENVINet-5 architecture that effectively extracts features from the dataset while being suitable for the classification of semi-arid regions. The three-dimensional input shape files such as patch size were fed to the ENVINet-5 model (Kumar et al., 2022; Rasheed & Mahmood, 2023; K. Zhang et al., 2023). Three-dimensional convolutional layers make up the proposed architecture. The first, second and third convolution layers involved the 16, 32, and 64 filters, respectively with the kernel size such as (2,2), and the stride such as (1,1).

Furthermore, two max-pooling layers with kernel size (2,2) have been utilized to decrease the spatial dimension and select the highest pixel value possible from the training dataset. The first dense layer had 64 neurons and the second dense layer had 128 neurons. A certified feature map is produced by the

ReLu after it completes each element operation with negative pixels equal to zero. The Softmax activation function was then applied to one output layer. The ENVINet-5 architecture is shown in Fig. 6. The number of epochs, loss function, learning rate, activation function, batch size, optimizer, and other parameters need to be set when using the ENVINet-5 architecture (Mohammadi et al., 2021; Singh et al., 2022b). The values of these parameters can significantly affect the precision of the classification. The parameters and their values are considered as (a) dropout=0.2, (b) learning rate=0.0002, (c) epochs=300, (d) batch size=128, and (e) activation function. To evaluate the performance of the ENVINet-5 architecture, an inbuilt toolbox is required which is provided by Environment for Visualizing Images (ENVI) software version 5.6 (Singh et al., 2021c). The hardware specifications required for the present work include Windows 10 or 11,8-16 GB RAM, NVIDIA Quadro P620 2 GB (4) MDP GFX. A total of 1000 samples are used in the model's training, out of which 80% are drawn from the training dataset and the rest 20% from the testing dataset. The training-based region of interest (ROI) is selected including a variety of classes such as wheat, water, buildup, fallow land, etc. After the model training, implementation is executed which generates classified maps of ENVINet-5 architecture. Classified maps are further processed to identify the changes in land use and land cover areas with the help of a suitable change detection technique (DCD).

Change detection

The change detection technique is used for identifying differences in an image or object taken on different dates via repeated observation (Dahiya et al., 2022). Numerous researchers have used various change detection approaches in the prior literature, including image differencing, image rationing, PCD, etc. Each method of change detection has benefits and disadvantages, and it is not suitable in all circumstances. However, the PCD technique has proven best among all techniques for the present work. There are numerous benefits of this method such as it can minimize the error caused by sensors and suitable for atmospheric differences. This approach also enables the pixel-by-pixel comparison of images and the classified map quality has a significant impact on accuracy. Numerous researchers have recommended this technique for LULC monitoring, agriculture, forest monitoring (Du et al., 2020; Mohammadi et al., 2021), and snow detection (Singh et al., 2022b).

Accuracy assessment

Accuracy evaluation is a vital stage in the processing of remote sensing data. Its primary goal is to examine how pixels were sampled into the proper land cover groups. By comparing the classifications created for each pixel to the specific land cover conditions found related to the ground truth data, the accuracy of the classified image is assessed. There are several parameters to measure the accuracy such as (a) producer accuracy (PA) which is the probability that reference pixels are correctly classified. It is represented as the compliment of omission error and is calculated as Producer's Accuracy = 100%-Omission Error. Omission errors are reference locations that were either omitted or left out of the right class on the classed map. (b) User accuracy (UA) refers to the pixels belonging to a specific class category. It is represented as the compliment of commission error and is calculated as User's Accuracy= 100%-Commission Error. It relates to classified sites that serve as references for locations that were incorrectly included in the appropriate class on the classified map. By looking for inaccurate classifications on the categorized sites, commission mistakes are computed. (c) Overall accuracy (OA) is utilized to determine the overall accuracy map for each class, (d) kappa coefficient (Kc) as demonstrated in Eq. (3) (Mohammadi & Sharifi, 2021; Sood et al., 2020) is defined as the difference between two agreements, namely, actual and expected. The range of the Kappa Coefficient is −1 to 1. A classification that is equal to a random classification is denoted by a value of 0. When the categorization is much poorer than random, a negative value is indicated. When the categorization is substantially better than random, the value is near to 1.

$$K_c = \frac{N \sum_{i=1}^{r} m_{ii} - \sum_{i=1}^{r} \left(Y_i L_i \right)}{N^2 - \sum_{i=1}^{r} \left(Y_i L_i \right)} \qquad (3)$$

The term K_c represents the value of the kappa coefficient; N shows the pixel count; r represents the rows and column count of the error's matrix; m_{ii} portrays the observation associated with class I; Y_i reflects the real values of class i whereas L_i displays

the anticipated values of class i. These metrics are useful in assessing a model's ability to classify or forecast unknown data with accuracy.

Result analysis

In the present work, the Landsat series datasets namely Landsat-7, Landsat-8, and Landsat-9 are used as input data. The Landsat-7 dataset was acquired from November 2012 to April 2013, the Landsat-8 dataset was acquired from November 2017 to April 2018, and the Landsat-9 dataset was acquired from November 2022 to April 2023 as shown in Fig. 4. Afterwards, ENVINet-5 architecture implementation is performed over the Landsat series dataset as shown in Fig. 5. The classification is done which generates classified maps of numerous categories represented as

wheat (with green color), water (with blue color), ripe wheat (with yellow color), buildup (with red color), and fallow land (with grey color) as shown in Fig. 6 and classification results have been shown in Fig. 7.

Various parameters, including error matrices, producer's accuracy, user's accuracy, and kappa value, are used to evaluate the accuracy assessment of the proposed algorithm. The accuracy assessment is done to evaluate the effectiveness of the ENVINet-5 architecture. Fine-resolution data from the Pléiades constellation—Pleiades -1A and Pléiades 1B—were used in the training and validation procedures. The Center National d'Etudes Spatiales (CNES)/Airbus Défense and Space oversees this satellite. It provides high-resolution photos that can give more specific information about the area. The integrated Google Earth (GE) viewer in the ERDAS Imagine Earth Resources Data Analysis System (2015) allows a picture to be
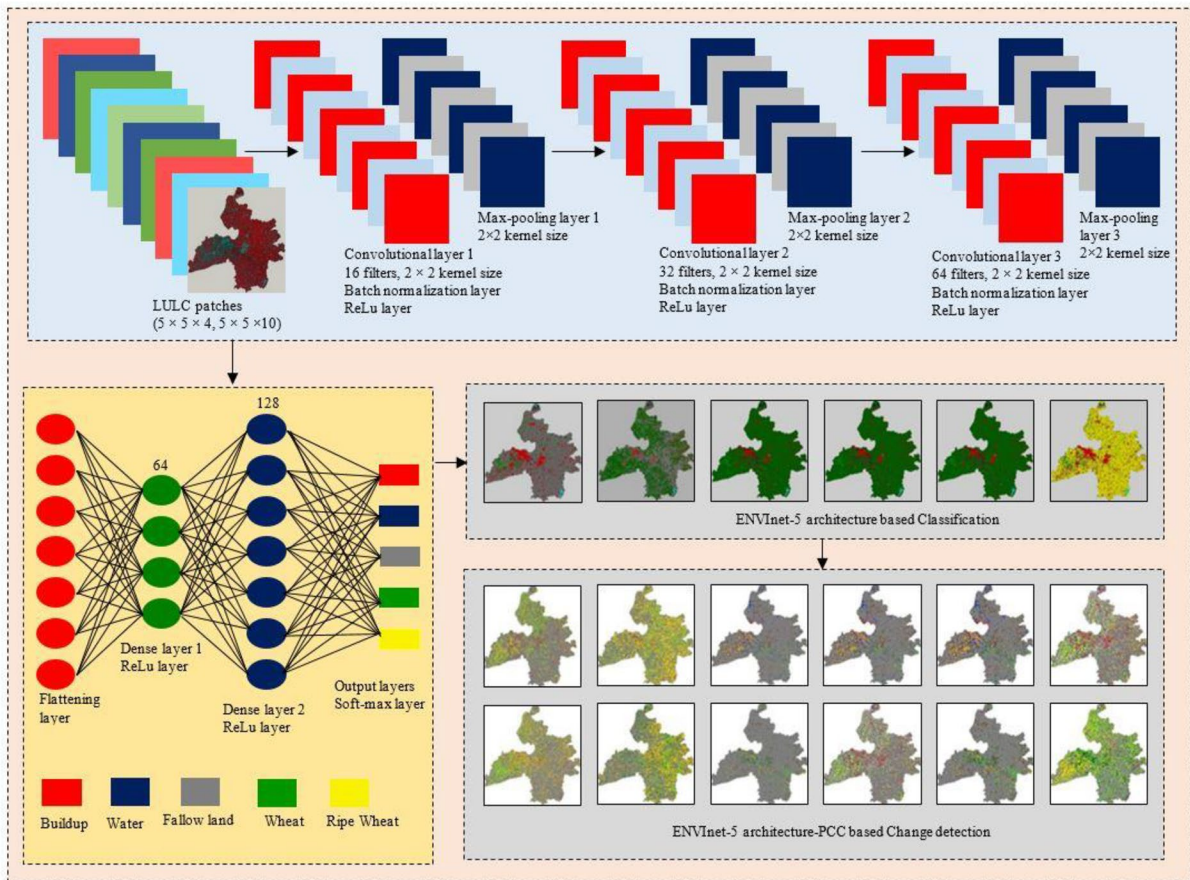
Fig. 5 The working flow diagram of ENVINet-5 architecture-based implementation
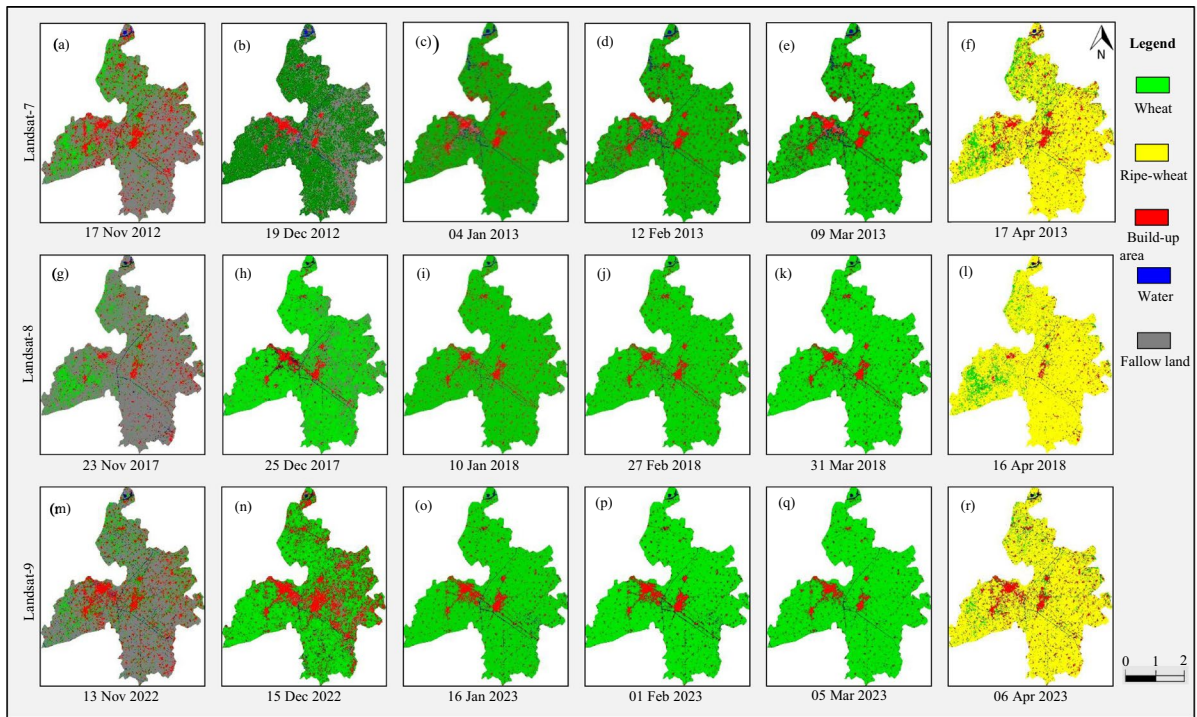
Fig. 6 Landsat-7 datasets classified maps on November 2012 to April 2013 (**a–f**), Landsat-8 datasets classified maps on November 2017 to April 2018 (**g–l**), and Landsat-9 datasets classified maps on November 2022 to April 2023 (**m–r**)
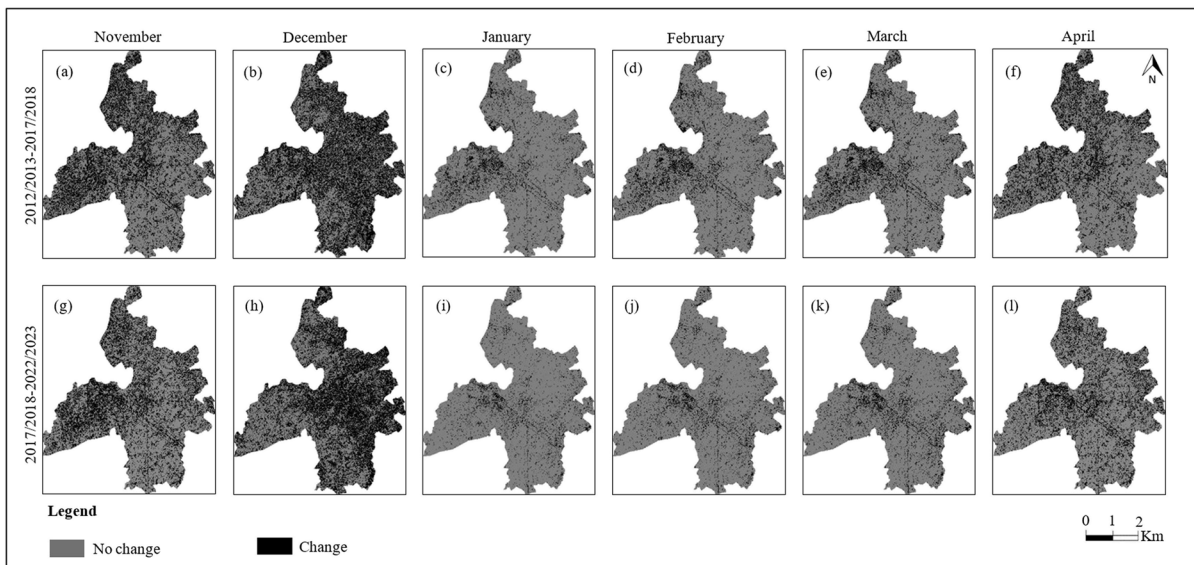
Fig. 7 Landsat-7 datasets to Landsat-8 datasets "change/no-change" change maps on November 2017 to April 2018 (**a–f**), and Landsat-8 datasets to Landsat-9 datasets "change/no-change" change maps on November 2022 to April 2023 (**g–l**)

anchored around the GE. It provides the capacity to establish a connection with GE, go to a designated place, match images with GE and vice versa, export prints, and carry out synchronizing.

Table 2 shows the accuracy assessment of the Landsat-7 dataset (89.4–90.2%) from Nov 2017 to Dec 2017 and (88–91.2%) from Jan 2018 to April 2018. Similarly, Table 3 reflects the accuracy assessment of the Landsat-8 dataset (86.8–91.4%) from Nov 2022 to Dec 2022 and (88.6–91.2%) from Jan 2023 to April 2023 and Table 4 shows Landsat-9 datasets accuracy of (90–92.8%) from Nov 2012 to Dec 2012 and accuracy of 91–93.2% from Jan 2013 to April 2013. The results show that the ENVINet-5 classifier

has achieved an accuracy of above 91% in all the cases and found that the suggested method produces more accurate results for Landsat data.

Afterwards, the classified map generated from the Landsat series dataset was used to generate the change maps. Figures 8 and 9 represent the 'from to change' map using the Landsat series dataset. The accuracy assessment of the changed map of ENVI-Net-5 architecture using Landsat-7 and Landsat-8 datasets has been shown in Tables 5 and 6. Similarly, the evaluation of the changed map of ENVINet-5 architecture for Landsat-8 and Landsat-9 datasets has been shown in Tables 7 and 8. The result depicts that ENVINet-5 architecture-based PCD is capable of

Table 2 Accuracy assessment of ENVINet-5 architecture of Landsat-7 dataset

Year	Month	Class categories	Accuracy assessment parameters					
			RT (%)	CT (%)	NC (%)	PA (%)	UA (%)	KC
2012	Nov	Wheat	22.4	21.6	21.8	88.2	90.7	0.88
		Buildup	24	22.4	23.4	89	94.6	0.92
		Water	21	20	19.9	85.7	90	0.87
		Fallow Land	32.6	36	34.9	96	87	0.81
		Overall Accuracy= 89.4%; Overall Kappa= 0.9289						
	Dec	Wheat	67	68.8	60.4	97.6	95	0.85
		Buildup	2.6	8.6	10.1	75.8	76.7	0.71
		Water	3.8	2.4	1.7	42.1	66.6	0.65
		Fallow Land	26.6	20.2	27.8	96.9	89.5	0.85
		Overall Accuracy= **90.2%;** Overall Kappa= 0.9486						
2013	Jan	Wheat	77.6	81.2	82.1	98.3	94	0.65
		Buildup	12.2	11.4	10.5	80.3	85.9	0.84
		Water	5	2	2.2	40	100	1.00
		Fallow Land	5.2	5.4	5.2	84.2	88	0.90
		Overall Accuracy= 88%; Overall Kappa= 0.9327						
	Feb	Wheat	74.4	74.9	75.1	98.5	92.1	0.58
		Buildup	13.2	11.4	17.4	75.3	85.9	0.83
		Water	7.6	8.5	2.5	33.3	100	1.0
		Fallow Land	4.8	5.2	5	86.4	94.2	0.87
		Overall Accuracy= 90.6%; Overall Kappa= 0.9264						
	Mar	Wheat	79	79.3	80.1	98.3	94.2	0.66
		Buildup	12	15.4	13.4	81.6	85.9	0.84
		Water	5	2.3	2.4	40	100	1.00
		Fallow Land	4	3	4.1	88.2	90	0.87
		Overall Accuracy= **92.4%;** Overall Kappa= 0.9357						
	April	Wheat	63.8	64.6	67.4	98.7	91.5	0.76
		Buildup	3.6	6.2	10.2	81.1	94.2	0.92
		Water	5	2.4	2.3	44	91.6	0.91
		Fallow Land	27.6	28.8	20.1	94.2	90.2	0.86
		Overall Accuracy= 91.2 %; Overall Kappa= 0.9306						

RT reference total, CT classified total, NC number of correct, PA producer's accuracy, UA user's accuracy, KC kappa coefficient

Table 3 Accuracy Assessment of ENVINet-5 architecture of Landsat-8 Dataset

Year	Month	Class categories	Accuracy assessment parameters					
			RT (%)	CT (%)	NC (%)	PA (%)	UA (%)	KC
2012	Nov	Wheat	9.4	7.6	7.4	73.9	89.4	0.88
		Buildup	5.8	3.4	3.2	51.7	88.2	0.87
		Water	3.6	1	1.3	27.7	100	1.0
		Fallow Land	81.2	88	88.1	99.2	91.5	0.55
		Overall Accuracy= **91.4%;** Overall Kappa= 0.6885						
	Dec	Wheat	61	70.6	69.8	99.3	85.8	0.63
		Buildup	9.4	5.6	5.2	48.9	82.1	0.80
		Water	5.4	1	1.1	14.8	80	0.78
		Fallow Land	24.2	22.8	23.9	86.6	91.2	0.88
		Overall Accuracy= 86.8%; Overall Kappa= 0.7406						
2013	Jan	Wheat	75.8	82.6	69.9	100	90.3	0.73
		Buildup	8.6	5.6	5.7	60.4	92.8	0.92
		Water	4.2	1	1.2	23.8	100	1.0
		Fallow Land	11.4	10.8	23.2	90.6	92.9	0.90
		Overall Accuracy= 91.2%; Overall Kappa= 0.8208						
	Feb	Wheat	61.2	70.6	69.8	50	86.1	0.64
		Buildup	9.2	5.6	5.2	14.8	82.1	0.80
		Water	5.4	1	101	99.3	80	0.78
		Fallow Land	24.2	22.8	23.9	86.7	91.2	0.88
		Overall Accuracy= 87%; Overall Kappa= 0.7439						
	Mar	Wheat	64.2	70.6	69.8	100	91.2	0.75
		Buildup	8.2	5.6	5.6	63.4	92.8	0.92
		Water	4.2	1	1.2	25	100	1.0
		Fallow Land	23.4	22.8	23.4	92.3	94.7	0.93
		Overall Accuracy= **92.2%;** Overall Kappa= 0.8398						
	April	Wheat	80.4	89.6	92.8	100	89.7	0.47
		Buildup	10.6	8.2	5.4	62.2	80.4	0.78
		Water	6	2.2	1.8	26.6	72.7	0.70
		Fallow Land	3	–	–	–	–	–
		Overall Accuracy= 88.6 %; Overall Kappa= 0.5772						

RT reference total, CT classified total, NC number of correct, PA producer's accuracy, UA user's accuracy, KC kappa coefficient

producing accuracy above 89% (approx.) for changed maps.

The representation of the changed area in percentage (%) is computed from the ENVINet-5 architecture using Landsat-7, Landsat-8, and Landsat-9 datasets which are shown in Tables 9 and 10. The results portray that agricultural land has been decreased and converted into urban areas (buildup) which is an alarming situation. ENVINet-5 architecture-based PCD has proven efficient in detecting changes in agricultural land. This work has shown that an ENVINet-5 architecture-based PCD improved the effectiveness of expanding the use of

the Landsat series dataset in the detection of land surface changes with a straightforward framework.

In this work, the potential of the ENVINET-5 has been explored on Landsat series datasets, i.e., Landsat-7, Landsat-8, and Landsat-9. The visual interpretation and statistical analysis confirm the effectiveness of the ENVINet-5 in the effective production of the classification maps as shown in Fig. 5. However, it has been noted that the accuracy of the Landsat-9 is only slightly greater than that of the Landsat-7 and Landsat-8. The primary cause of such results may involve the better radiometric resolution (14-bit) offered by the Landsat-9 as compared

Table 4 Accuracy assessment of ENVINet-5 architecture of Landsat-9 dataset

| Year	Month	Class categories	Accuracy assessment parameters					
			RT (%)	CT (%)	NC (%)	PA (%)	UA (%)	KC
2012	Nov	Wheat	10.6	9.2	9.1	82.6	93.4	0.92
		Buildup	13.2	11.8	11.7	84.6	93.2	0.92
		Water	2.8	1	1.2	35.7	100	1.0
		Fallow Land	73.4	78	78	100	94.1	0.77
		Overall Accuracy= 90%; Overall Kappa= 0.8509						
	Dec	Wheat	65.8	69.6	70.2	99	93.6	0.81
		Buildup	20.8	20	19.6	87.5	91	0.88
		Water	4.8	1.6	1.4	27.2	75	0.73
		Fallow Land	8.6	8.8	8.8	97.6	93.1	0.92
		Overall Accuracy= **92.8%;** Overall Kappa= 0.8538						
2013	Jan	Wheat	83.8	88.4	89	100	93.5	0.60
		Buildup	9.8	8.2	7	75.5	90.2	0.89
		Water	4.2	2.2	2.1	47.6	90.9	0.90
		Fallow Land	2.2	1.2	1.9	86.4	91.2	0.88
		Overall Accuracy= 93.2%; Overall Kappa= 0.7169						
	Feb	Wheat	83	86.6	87.8	100	92.6	0.56
		Buildup	10	8.2	8	74	90.2	0.89
		Water	4.4	2.2	2	45.4	90.9	0.90
		Fallow Land	2.6	3	2.2	99.2	79.2	0.56
		Overall Accuracy= 92.4%; Overall Kappa= 0.6925						
	Mar	Wheat	85.6	86.6	86.3	100	95.5	0.69
		Buildup	9.2	8.2	8.3	57.8	97.5	0.97
		Water	3.8	2.2	2.2	86.9	100	1.0
		Fallow Land	0.4	3	3.4	96.7	92.4	0.78
		Overall Accuracy= **95.8%;** Overall Kappa= 0.8130						
	April	Wheat	81.8	88.6	88.8	100	91.2	0.52
		Buildup	10.6	8	8.4	69.8	90.2	0.89
		Water	4.6	2.2	1.8	39.1	81.8	0.80
		Fallow Land	3	1.2	1.1	57.6	91.4	0.90
		Overall Accuracy= 91 %; Overall Kappa= 0.6503						

RT reference total, CT classified total, NC number of correct, PA producer's accuracy, UA user's accuracy, KC kappa coefficient

to the Landsat-8 (12-bit) and Landsat-7 (8-bit) as shown in Figs. 9, 10 and 11. This is one of the important parameters of the sensor which allows the better detection of smaller differences in the energy reflected from the object. It has also been observed that the errors in the results are still high which needs to be improved with the help of the improvement in the preprocessing steps, better feature selection during the classification process, and advanced models for the detection of minor changes or least impacted with the classification outcomes. The Landsat series is one of the important platforms for the detection of long-term changes. Future studies may involve the integration of artificial intelligence (AI) driven models for the accurate monitoring of land cover changes.

Discussion

To evaluate the utility of DCD algorithm over agriculture area, validation has been done using Landsat series dataset. In past literature, the U-Net algorithm has been used over glacier lakes by using Landsat dataset and achieved accuracy of 85.3% (He et al., 2021; Marzvan et al., 2021). Similarly, U-Net classifier is used for irrigation mapping over Montana state from 2000 to 2019 using
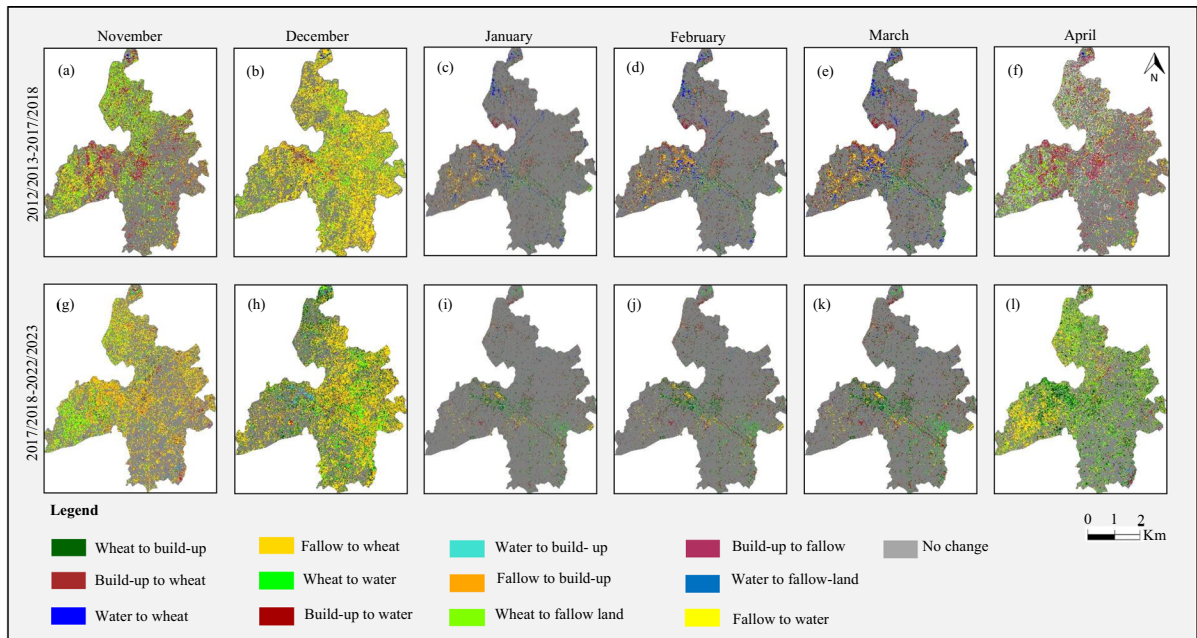
Fig. 8 Landsat-7 datasets to Landsat-8 datasets "from-to" change maps on November 2017 to April 2018 (**a–f**), and Landsat-8 datasets to Landsat-9 datasets "from-to" change maps on November 2022 to April 2023 (**g–l**)
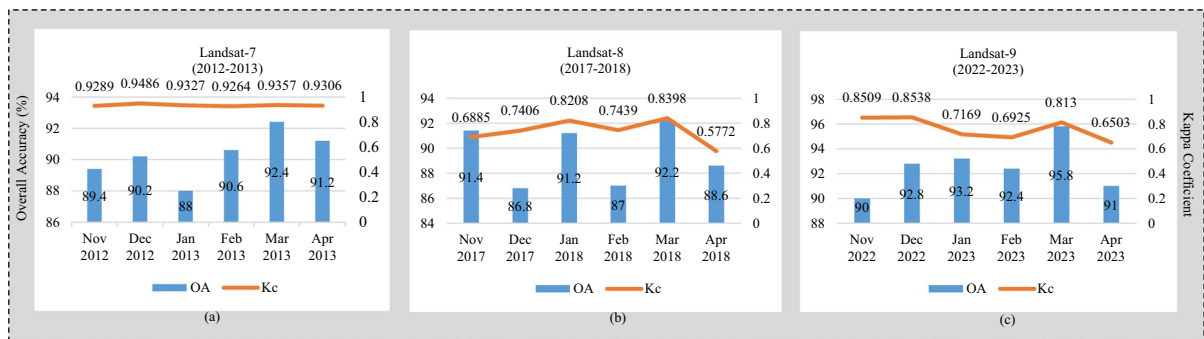
Fig. 9 Comparison of accuracy assessment of classified maps computed from (**a**) Landsat-7 (2012–2013), (**c**) Landsat-8 (2017–2018), and Landsat-9 (2022–2023).

Landsat dataset (Colligan et al., 2022; Mohammadi et al., 2021). Singh et al. use machine learning algorithm for LULC detection using Landsat series dataset and achieved accuracy below 86%. Similarly, Zhang et al. (2022) suggested a continuous change detection strategy to monitor the forest utilizing a multispectral dataset using an index method over the country of China with three categories and achieved accuracy of 86.4%. As comparative to previous studies, our model performs better than other approaches used. The primary goal of this research is to use proposed algorithm to create an effective and realistic change detection method. Specifically, this algorithm is designed to highlight the agriculture classes and their variations using Landsat series datasets. Deep learning algorithm has been applied to attain state-of-the-art performance on a variety of tasks and is also capable of handling big and complicated data. But, to train, it needs a lot of data and

Table 5 Accuracy assessment (PA, UA, KC) of ENVINet-5 architecture -PCD change map using Lansat-7 and Landsat-8

Year		2012–2017			2012–2017			2013–2018			2013–2018			2013–2018			2013–2018		
Month		Nov			Dec			Jan			Feb			Mar			Apr		
S. No.	Change classes	PA (%)	UA (%)	KC	PA (%)	UA (%)	KC	PA (%)	UA (%)	KC	PA (%)	UA (%)	KC	PA (%)	UA (%)	KC	PA (%)	UA (%)	KC
1	Wheat- Buildup	12.5	100	1.0	–	–	–	65.7	95.8	0.95	67.6	95.8	0.95	77.1	96.4	0.96	12.5	100	1.0
2	Wheat- Water	75.5	94.8	0.94	54.5	85.7	0.85	96	90.6	0.86	96.5	92.2	0.89	96.2	91.4	0.88	75	92.3	0.91
3	Wheat- Fallow Land	97.7	90.5	0.86	38.8	87.5	0.87	–	–	–	–	–	–	–	–	–	97.6	88.1	0.83
4	Buildup- Wheat	–	–	–	20	100	1.0	31.2	100	1.0	38.4	100	1.0	38.4	83.3	0.83	–	–	–
5	Buildup- Water	18.7	75	0.74	20	100	1.0	63.3	86.3	0.85	72.4	95.4	0.95	73.9	94.4	0.94	14.2	75	0.74
6	Buildup- Fallow Land	14.2	66	0.66	50	100	1.0	–	–	–	–	–	–	–	–	–	11.1	66	0.66
7	Water- Wheat	20	100	1.0	95.9	90.4	0.88	97.3	88.6	0.83	98.3	90.7	0.86	98	91	0.87	20	100	1.0
8	Water- Buildup	14.2	66.6	0.66	65.3	89.4	0.89	94	91.2	0.89	94.6	92.4	0.9	95.5	92.2	0.90	14.2	66.6	0.66
9	Water- Fallow Land	98.3	90.5	0.85	95.3	90.4	0.88	15.3	100	1.0	18.1	100	1.0	22.2	100	1.0	98.3	89.7	0.84
10	Fallow Land- Wheat	95	88.3	0.87	100	90.5	0.88	100	84.8	0.84	100	87.8	0.87	84.6	93.6	0.93	95	88.3	0.87
11	Fallow Land- Buildup	100	70	0.69	100	88.8	0.88	100	100	1.0	100	100	1.0	50	100	1.0	100	70	0.69
12	Fallow Land- Water	100	87.2	0.85	100	92.4	0.88	100	93.1	0.92	100	93.1	0.92	97.5	90.5	0.89	100	86.1	0.83
		OA=89.7%			OA=91.2%			OA=90.3%			**OA=92%**			OA=91.6%			OA=88.3%		
		OK=0.8587			OK=0.8869			OK=0.8746			**OK=0.8962**			OK=0.8923			OK=0.8404		

PA producer's accuracy, UA user's accuracy, OA overall accuracy, KC kappa coefficient

Table 6 Accuracy assessment (RT, CT, NC) of ENVINet-5 architecture -PCD change map using Landsat-7 and Landsat-8

| Year | 2012–2017 | | | 2012–2017 | | | 2013–2018 | | | 2013–2018 | | | 2013–2018 | | | 2013–2018 | | |
| Month | Nov | | | Dec | | | Jan | | | Feb | | | Mar | | | Apr | | |
S. No. Change classes	RT (%)	CT (%)	NC (%)	RT (%)	CT (%)	NC (%)	RT (%)	CT (%)	NC (%)	RT (%)	CT (%)	NC (%)	RT (%)	CT (%)	NC (%)	RT (%)	CT (%)	NC (%)
1 Wheat- Buildup	1.6	0.2	0.2	1.3	–	–	3.5	2.4	2.5	3.4	2.4	2.5	3.5	2.8	2.9	1.6	0.2	0.2
2 Wheat- Water	4.9	3.9	4.5	2.2	1.4	1.3	28.1	29.8	29.9	28.6	29.8	29.8	26.6	28	27.9	4.8	3.9	4
3 Wheat- Fallow Land	30.5	32.9	33.2	1.8	0.8	0.7	1.2	–	–	0.9	–	–	1.1	–	–	29.7	32.9	32.8
4 Buildup- Wheat	1.3	–	–	1.5	0.3	0.3	1.6	0.5	0.5	1.3	0.5	0.5	1.3	0.6	0.5	1.8	–	–
5 Buildup- Water	1.6	0.4	0.3	1	0.2	0.2	3	2.2	2.1	2.9	2.2	2.2	2.3	1.8	1.7	2.1	0.4	0.3
6 Buildup- Fallow Land	1.4	0.3	0.2	2	1	2	1.1	–	–	1	–	–	0.6	–	–	1.8	0.3	0.2
7 Water- Wheat	1.5	0.3	0.3	19.8	21	20	30.4	33.4	32.7	30.8	33.4	32.9	31.2	33.6	33.4	1.5	0.3	0.3
8 Water- Buildup	1.4	0.3	0.2	2.6	1.9	1.8	16.7	17.2	17.3	16.8	17.2	17.2	13.6	14.1	14.1	1.4	0.3	0.2
9 Water- Fallow Land	36	39.1	39.4	14.9	15.7	15.5	1.3	0.2	0.6	1.1	0.2	0.7	0.9	0.2	0.2	35.7	39.1	39.7
10 Fallow Land- Wheat	4	4.3	4.2	20.1	22.2	22	2.8	3.3	3.1	2.9	3.3	3.1	5.2	4.7	4.8	4	4.3	4.3
11 Fallow Land- Buildup	0.7	1	0.7	0.8	0.9	0.8	0.8	0.8	0.8	0.8	0.8	0.8	1	0.5	1	0.7	1	0.5
12 Fallow Land- Water	15.1	17.3	16.8	32	34.6	35.4	9.5	10.2	10.5	9.5	10.2	10.3	12.7	13.7	13.5	14.9	17.3	15.7

RT reference total, CT classified total, NC number of correct

Table 7 Accuracy assessment (PA, UA, KC) of ENVINet-5 architecture -PCD change map using Lansat-8 and Landsat-9

Year		2017–2022			2017–2022			2018–2023			2018–2023			2018–2023			2018–2023		
Month		NOV			DEC			JAN			FEB			MAR			APR		
S. No.	Change classes	PA (%)	UA (%)	KC	PA (%)	UA (%)	KC	PA (%)	UA (%)	KC	PA (%)	UA (%)	KC	PA (%)	UA (%)	KC	PA (%)	UA (%)	KC
1	Wheat-Buildup	–	–	–	12.5	100	1.0	79.4	96.4	0.96	77.1	96.4	0.96	71.8	95.8	0.95	12.5	100	1.0
2	Wheat-Water	47.8	78.5	0.78	75	92.3	0.91	97.4	93.5	0.91	96.9	91.4	0.88	96.8	92.6	0.89	75.5	94.8	0.94
3	Wheat-Fallow Land	35	87.5	0.87	97.6	89	0.84	–	–	–	–	–	–	–	–	–	97.7	90.5	0.86
4	Buildup-Wheat	17.6	100	1.0	–	–	–	41.6	83.3	0.83	38.4	83.3	0.83	38.4	100	1.0	–	–	–
5	Buildup-Water	16.6	100	1.0	15	75	0.74	70.8	94.4	0.94	73.9	94.4	0.94	72.4	95.4	0.95	18.7	75	0.74
6	Buildup-Fallow Land	45.4	100	1.0	11.7	66.6	0.66	–	–	–	–	–	–	–	–	–	14.2	66.6	0.66
7	Water-Wheat	95.9	89.5	0.86	20	100	1.0	98.4	92.8	0.89	98	91	0.87	98	90.7	0.86	20	100	1.0
8	Water-Buildup	65.3	89.4	0.89	14.2	66.6	0.66	97	92.2	0.90	95.5	92.2	0.90	94.1	93	0.91	14.2	66.6	0.66
9	Water-Fallow Land	95.2	89.1	0.87	98.3	89.7	0.84	28.5	100	1.0	22.2	100	1.0	18.1	100	1.0	98.3	90.7	0.85
10	Fallow Land-Wheat	100	89.6	0.87	95	88.3	0.87	89.8	93.6	0.93	84.6	93.6	0.93	100	87.8	0.87	100	88.3	0.87
11	Fallow Land-Buildup	100	88.8	0.88	100	70	0.69	57.1	80	0.79	50	100	1.0	100	100	1.0	100	70	0.69
12	Fallow Land-Water	100	91	0.86	100	86.1	0.83	98.5	95.6	0.94	97.6	91.9	0.90	100	93.1	0.92	100	87.8	0.85
		OA=90%			OA=88.6%			**OA=93.4%**			OA=91.8%			OA=92.2%			OA=89.9%		
		OK=0.8720			OK=0.8443			**OK=0.9151**			OK=0.8949			OK=0.8988			OK=0.8613		

PA producer's accuracy, UA user's accuracy, OA overall accuracy, KC kappa coefficient

Table 8 Accuracy assessment (RT, CT, NC) of ENVINet-5 architecture -PCD change map using Landsat-8 and Landsat-9

Year		2017–2022			2017–2022			2018–2023			2018–2023			2018–2023			2018–2023		
Month		Nov			Dec			Jan			Feb			Mar			Apr		
S. No.	Change classes	RT (%)	CT (%)	NC (%)	RT (%)	CT (%)	NC (%)	RT (%)	CT (%)	NC (%)	RT (%)	CT (%)	NC (%)	RT (%)	CT (%)	NC (%)	RT (%)	CT (%)	NC (%)
1	Wheat–Buildup	1.5	–	–	1.6	0.2	0.2	3.4	2.8	2.8	3.5	2.8	1.2	3.2	2.4	2.4	1.6	0.2	0.2
2	Wheat–Water	2.3	1.4	1.2	4.8	3.9	4.0	26.9	28	28	26.4	28	0.7	28.5	29.8	29.9	4.9	3.9	4.1
3	Wheat–Fallow Land	2	0.8	0.7	30	32.9	33	0.9	–	–	1.1	–	–	0.9	–	–	30.5	32.9	33.1
4	Buildup–Wheat	1.7	0.3	0.3	1.7	–	–	1.2	0.6	0.5	1.3	0.6	0.3	1.3	0.5	0.5	1.3	–	–
5	Buildup–Water	1.2	0.2	0.2	2	0.4	0.3	2.4	1.8	1.8	2.3	1.8	0.2	2.9	2.2	2.2	1.6	0.4	0.3
6	Buildup–Fallow Land	2.2	1	1.1	1.7	0.3	0.2	0.5	–	–	0.6	–	–	1	–	–	1.4	0.3	0.2
7	Water–Wheat	19.6	21	20.8	1.5	0.3	0.3	31.7	33.6	33.4	31.2	33.6	1.1	30.9	33.4	32.8	1.5	0.3	0.3
8	Water–Buildup	2.6	1.9	1.8	1.4	0.3	0.7	13.4	14.1	13.9	13.6	14.1	20.8	17	17.2	17.3	1.4	0.3	0.2
9	Water–Fallow Land	14.7	15.7	15.5	35.7	39.1	39.6	0.7	0.2	0.5	0.9	0.2	1.8	1.1	0.2	0.7	36.1	39.1	39.4
10	Fallow Land–Wheat	19.9	22.2	22.6	4	4.3	4.2	4.9	4.7	4.7	5.2	4.7	15.5	2.9	3.3	3.1	3.8	4.3	4.8
11	Fallow Land–Buildup	8	0.9	0.8	0.7	1	0.7	0.7	0.5	0.4	1	0.5	22.6	0.8	0.8	0.8	0.7	1	0.7
12	Fallow Land–Water	31.5	34.6	35	14.9	14.9	16.8	13.3	13.7	14	12.9	3.7	35.8	9.5	10.2	10.3	15.2	17.3	16.9

RT reference total, CT classified total, NC number of correct

Table 9 Representation of change area (in percentage) computed from the ENVINet-5 architecture using Landsat-7 and Landsat-8

S. No.	Change classes	2012–2017 Nov	2012–2017 Dec	2013–2018 Jan	2013–2018 Feb	2013–2018 Mar	2013–2018 Apr
1	Wheat to Buildup	0.50%	0.10%	0.03%	0.20%	0.50%	88.22%
2	Wheat to Water	3.20%	0.20%	2.12%	2.22%	2.50%	0.05%
3	Wheat to Fallow Land	1.00%	0.35%	0.05%	0.50%	1.00%	0.59%
4	Buildup to Wheat	0.50%	0.03%	0.08%	0.80%	0.10%	3.20%
5	Buildup to Water	0.30%	0.40%	0.84%	0.84%	0.50%	0.01%
6	Buildup to Fallow Land	0.20%	0.09%	0.02%	0.10%	0.70%	0.06%
7	Water to Wheat	0.06%	0.21%	1.18%	1.10%	1.60%	0.07%
8	Water to Buildup	2.40%	0.16%	0.17%	0.20%	0.17%	0.22%
9	Water to Fallow Land	0.60%	3.86%	0.27%	0.25%	1.20%	0.06%
10	Fallow Land to Wheat	0.10%	0.91%	0.17%	0.17%	0.10%	4.48%
11	Fallow Land to Buildup	2.10%	0.25%	0.01%	0.05%	0.12%	0.74%
12	Fallow Land to Water	0.50%	10.36%	0.59%	0.59%	0.50%	0.16%

Table 10 Representation of change area (in percentage) computed from the ENVINet-5 architecture using Landsat-8 and Landsat-9

S. No.	Change classes	2012–2017 Nov	2012–2017 Dec	2013–2018 Jan	2013–2018 Feb	2013–2018 Mar	2013–2018 APR
1	Wheat to Buildup	0.50%	0.01%	0.15%	0.50%	0.70%	0.05%
2	Wheat to Water	1.50%	0.23%	1.20%	2.50%	2.02%	0.59%
3	Wheat to Fallow Land	2.70%	0.20%	0.00%	1.00%	0.50%	3.20%
4	Buildup to Wheat	1.30%	0.16%	0.03%	0.10%	0.80%	0.01%
5	Buildup to Water	0.40%	0.21%	0.16%	0.50%	0.16%	0.06%
6	Buildup to Fallow Land	0.60%	0.14%	0.00%	0.70%	0.10%	0.07%
7	Water to Wheat	0.20%	3.74%	1.09%	1.60%	1.10%	0.22%
8	Water to Buildup	0.60%	0.40%	0.64%	0.64%	0.20%	0.06%
9	Water to Fallow Land	2.10%	2.89%	0.05%	1.20%	0.25%	4.47%
10	Fallow Land to Wheat	1.60%	3.41%	0.08%	0.10%	0.08%	0.74%
11	Fallow Land to Buildup	0.90%	0.11%	0.02%	0.12%	0.05%	0.16%
12	Fallow Land to Water	1.20%	5.45%	0.33%	0.50%	0.33%	2.13%

processing power, which makes it computationally costly. In the current study, a deep learning-based change detection (DCD) algorithm has been proposed to detect long-term agricultural changes using the Landsat series datasets (i.e., Landsat-7, Landsat-8, and Landsat-9) during the period 2012 to 2023. The proposed algorithm extracts feature from satellite data according to their spectral and geographic characteristics and identifies seasonal variability.
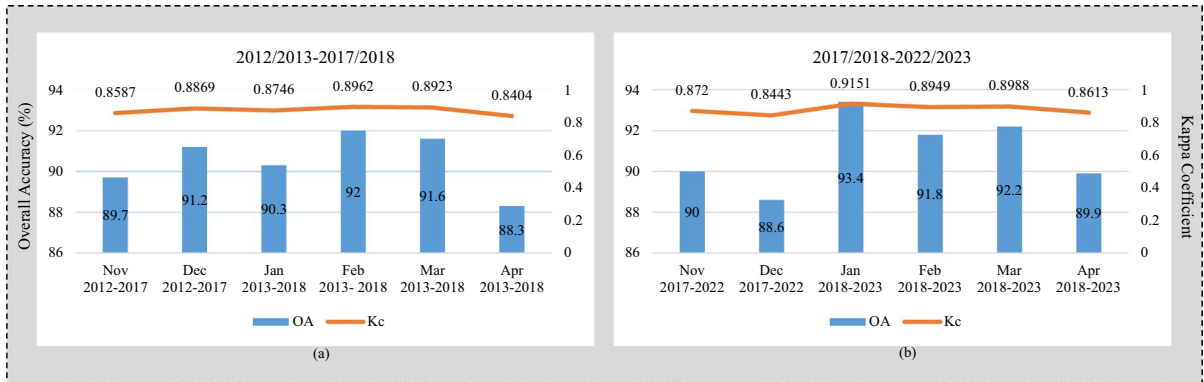
Fig. 10 Comparison of accuracy assessment of change maps computed from (**a**) Landsat-7 to Landsat-8 (2012/2013-2017–2018), and (**b**) Landsat-8 to Landsat-9 (2017/2018–2022/2023)

Fig. 11 Graphical representation of "change and no-change" area computed from (**a**) Landsat-7 to Landsat-8 (2012/2013-2017–2018), and (**b**) Landsat-8 to Landsat-9 (2017/2018–2022/2023).

The visual interpretation and statistical analysis confirm the effectiveness of the ENVINet-5 in the effective production of the classification maps as shown in Tables 1, 2, 3 and Fig. 5. However, it has been noted that the accuracy of the Landsat-9 is only slightly greater than that of the Landsat-7 and Landsat-8. The primary cause of such results may involve the better radiometric resolution (14-bit) offered by the Landsat-9 as compared to the Landsat-8 (12-bit) and Landsat-7 (8-bit) as shown in Figs. 8, 9 and 10. According to the experimental results, vegetation has declined between 2012 and 2023, but buildup land has been expanded to 88.22% between 2012 and 2023 for the Landsat-7 and Landsat-8 datasets. Conversely, fallow land (1–0.59%) and water (3.20–0.05%) make up the degraded area. This research's primary objective is

to categorize agricultural land using a deep learning-based classifier, such as the ENVINet-5 architecture, and use the DCD approach to monitor changes over time. Additionally, it is determined that by utilizing the Landsat series information, the design has the potential to increase accuracy.

Conclusion and future scope

This work evaluates the potential of the DCD architecture over an agricultural area, i.e. Fatehgarh Sahib, Punjab using the Landsat series dataset. The results make it clear that the proposed model can increase the accuracy of LULC categorization and agriculture monitoring. The data is categorized as wheat, ripe wheat, buildup, water, and fallow land.

The experimental result concludes that vegetation has decreased from 2012 to 2023, while buildup land has increased up to 88.22% (2012–2023) for Landsat-7 and Landsat-8 datasets. On the other side, degraded area includes water (3.20–0.05%) and fallow land (1–0.59%). The main goal of this research is to implement a deep learning-based classifier, i.e., ENVINet-5 architecture to classify the agricultural land and measure the changes using the DCD technique. It is also concluded that the architecture also has the potential to improve the accuracy using the Landsat series dataset. Although significant progress has been achieved in change detection, there are still many obstacles because of factors including lack of training data and previous knowledge. Moreover, a lot of fundamental problems with remote sensing datasets that haven't been addressed yet, such as heterogeneous data, multiresolution pictures, and global information of high-resolution and large-scale images. Thus, it is highly recommended to do more research with a greater emphasis on these issues. This study will be helpful in the identification of crop growth, crop yield prediction, precision farming, and crop mapping. Additionally, it is also expected that this study will provide direction and practical guidance to researchers and scientists.

Dataset availability The Landsat series dataset can be downloaded from the online web portal (https://earthexplorer.usgs.gov/).

Declarations

Ethics approval All authors have read, understood, and have complied as applicable with the statement on "Ethical responsibilities of Authors" as found in the Instructions for Authors.

Conflict of interest The authors declare no competing interests.

References

Al-Dousari, A. E., Mishra, A., & Singh, S. (2023). Land use land cover change detection and urban sprawl prediction for Kuwait metropolitan region, using multi-layer perceptron neural networks (MLPNN). *The Egyptian Journal of Remote Sensing and Space Science, 26*(2), 381–392.

Alshari, E. A., Abdulkareem, M. B., & Gawali, B. W. (2023). Classification of land use/land cover using artificial intelligence (ANN-RF). *Frontiers in Artificial Intelligence, 5*, 964279.

Bali, N., & Singla, A. (2021). Deep learning based wheat crop yield prediction model in Punjab Region of North India. *Applied Artificial Intelligence, 35*, 1–25. https://doi.org/10.1080/08839514.2021.1976091

Basheer, S., Wang, X., Farooque, A. A., Nawaz, R. A., Liu, K., Adekanmbi, T., & Liu, S. (2022). Comparison of land use land cover classifiers using different satellite imagery and machine learning techniques. *Remote Sensing, 14*(19), 4978.

Boonpook, W., Tan, Y., Nardkulpat, A., Torsri, K., Torteeka, P., Kamsing, P., Sawangwit, U., Pena, J., & Jainaen, M. (2023). Deep learning semantic segmentation for land use and land cover types using Landsat 8 imagery. *ISPRS International Journal of Geo-Information, 12*(1), 14.

Chen, H., Wu, C., Du, B., Zhang, L., & Wang, L. (2019). Change detection in multisource VHR images via deep siamese convolutional multiple-layers recurrent neural network. *IEEE Transactions on Geoscience and Remote Sensing, 58*(4), 2848–2864.

Colligan, T., Ketchum, D., Brinkerhoff, D., & Maneta, M. (2022). A deep learning approach to mapping irrigation using Landsat: IrrMapper U-Net. *IEEE Transactions on Geoscience and Remote Sensing, 60*, 1–11. https://doi.org/10.1109/TGRS.2022.3175635

Dahiya, N., Gupta, S., & Singh, S. (2022). A review paper on machine learning applications, advantages, and techniques. *ECS Transactions, 107*(1), 6137–6150. https://doi.org/10.1149/10701.6137ecst

Dahiya, N., Singh, S., & Gupta, S. (2023). A review on deep learning classifier for hyperspectral imaging. *International Journal of Image and Graphics, 23*(04), 2350036.

Dibs, H., Ali, A. H., Al-Ansari, N., & Abed, S. A. (2023). Fusion Landsat-8 thermal TIRS and OLI datasets for superior monitoring and change detection using remote sensing. *Emerging Science Journal, 7*(2), 428–444.

Du, P., Wang, X., Chen, D., Liu, S., Lin, C., & Meng, Y. (2020). An improved change detection approach using tri-temporal logic-verified change vector analysis. *ISPRS Journal of Photogrammetry and Remote Sensing, 161*(December 2019), 278–293. https://doi.org/10.1016/j.isprsjprs.2020.01.026

e Silva, L. P., Xavier, A. P. C., da Silva, R. M., & Santos, C. A. G. (2020). Modeling land cover change based on an artificial neural network for a semiarid river basin in northeastern Brazil. *Global Ecology and Conservation, 21*, e00811.

Esmaeili, M., Abbasi-Moghadam, D., Sharifi, A., Tariq, A., & Li, Q. (2023). Hyperspectral image band selection based on CNN embedded GA (CNNeGA). *IEEE Journal of Selected Topics in Applied Earth Observations and Remote Sensing, 16*, 1927–1950. https://doi.org/10.1109/JSTARS.2023.3242310

Eugene, G. Y., Di, L., Meyer, D. J., Zhao, P., Lin, L., Zhang, C., & Cvejovic, S. (2022). ICroplandNet: An open distributed training dataset for irrigated cropland detection. In *2022 10th International Conference on Agro-Geoinformatics (Agro-Geoinformatics)* (pp. 1–6).

Farmonov, N., Amankulova, K., Szatmari, J., Sharifi, A., Abbasi-Moghadam, D., Mirhoseini Nejad, S. M., & Mucsi, L. (2023). Crop type classification by DESIS hyperspectral imagery and machine learning algorithms. *IEEE Journal of Selected Topics in Applied Earth Observations and Remote Sensing*, 1–17. https://doi.org/10.1109/JSTARS.2023.3239756

Felegari, S., Sharifi, A., Khosravi, M., & Sabanov, S. (2023). Using experimental models and multitemporal Landsat-9 images for cadmium concentration mapping. *IEEE Geoscience and Remote Sensing Letters, 20*, 1–4. https://doi.org/10.1109/LGRS.2023.3291019

Goswami, A., Sharma, D., Mathuku, H., Gangadharan, S. M. P., Yadav, C. S., Sahu, S. K., Pradhan, M. K., Singh, J., & Imran, H. (2022). Change detection in remote sensing image data comparing algebraic and machine learning methods. *Electronics (Switzerland), 11*(3), 1–26. https://doi.org/10.3390/electronics11030431

Gusain, H. S., Negi, H. S., Dhamija, S., Mishra, V. D., & Snehmani. (2019). Development of avalanche information system using remote sensing and GIS technology in the Indian Karakoram Himalaya. *Current Science, 117*(1), 104.

He, Y., Yao, S., Yang, W., Yan, H., Zhang, L., Wen, Z., Zhang, Y., & Liu, T. (2021). An extraction method for glacial lakes based on Landsat-8 imagery using an improved U-Net network. *IEEE Journal of Selected Topics in Applied Earth Observations and Remote Sensing, 14*, 6544–6558. https://doi.org/10.1109/JSTARS.2021.3085397

Henry, C. J., Storie, C. D., Palaniappan, M., Alhassan, V., Swamy, M., Aleshinloye, D., Curtis, A., & Kim, D. (2019). Automated LULC map production using deep neural networks. *International Journal of Remote Sensing, 40*(11), 4416–4440.

Ienco, D., Gaetano, R., Dupaquier, C., & Maurel, P. (2017). Land cover classification via multitemporal spatial data by deep recurrent neural networks. *IEEE Geoscience and Remote Sensing Letters, 14*(10), 1685–1689. https://doi.org/10.1109/lgrs.2017.2728698

Jalayer, S., Sharifi, A., Abbasi-Moghadam, D., Tariq, A., & Qin, S. (2023). Assessment of spatiotemporal characteristic of droughts using in situ and remote sensing-based drought indices. *IEEE Journal of Selected Topics in Applied Earth Observations and Remote Sensing, 16*,

1483–1502. https://doi.org/10.1109/JSTARS.2023.3237380

Jozdani, S. E., Johnson, B. A., & Chen, D. (2019). Comparing deep neural networks, ensemble classifiers, and support vector machine algorithms for object-based urban land use/land cover classification. *Remote Sensing, 11*(14), 1–24. https://doi.org/10.3390/rs11141713

Kaur, R., Tiwari, R. K., Maini, R., & Singh, S. (2023). A framework for crop yield estimation and change detection using image fusion of microwave and optical satellite dataset. *Quaternary, 6*(2). https://doi.org/10.3390/quat6020028

Kaur, S., Gupta, S., Singh, S., & Gupta, I. (2022). Detection of Alzheimer's disease using deep convolutional neural network. *International Journal of Image and Graphics, 22*(03), 2140012.

Kumar, S., Arya, S., & Jain, K. (2022). A SWIR-based vegetation index for change detection in land cover using multitemporal Landsat satellite dataset. *International Journal of Information Technology*, 1–14. https://doi.org/10.1007/s41870-021-00797-6

Kumar, S., & Jain, K. (2020). A multi-temporal Landsat data analysis for land-use/land-cover change in Haridwar Region using remote sensing techniques. *Procedia Computer Science, 171*, 1184–1193. https://doi.org/10.1016/j.procs.2020.04.127

Liang, Y., Zhang, W., Wang, B., Zheng, Z., Xu, J., Wang, H., & Xu, X. (2022). A more effective way of target segmentation of multispectral imaging data using Kmeans algorithm. In *2022 7th Asia-Pacific Conference on Intelligent Robot Systems (ACIRS)* (pp. 82–88).

Lu, D., Li, G., & Moran, E. (2014). Current situation and needs of change detection techniques. *International Journal of Image and Data Fusion, 5*(1), 13–38. https://doi.org/10.1080/19479832.2013.868372

Lu, D., Mausel, P., Brondízio, E., & Moran, E. (2004). Change detection techniques. *International Journal of Remote Sensing, 25*(12), 2365–2401. https://doi.org/10.1080/0143116031000139863

Mahmoud, R., Hassanin, M., Al Feel, H., & Badry, R. M. (2023). Machine learning-based land use and land cover mapping using multi-spectral satellite imagery: A case study in Egypt. *Sustainability, 15*(12), 9467.

Marzvan, S., Moravej, K., Felegari, S., Sharifi, A., & Askari, M. S. (2021). Risk assessment of alien Azolla filiculoides Lam in Anzali Lagoon using remote sensing imagery. *Journal of the Indian Society of Remote Sensing, 49*(8), 1801–1809. https://doi.org/10.1007/s12524-021-01362-1

Mishra, V. D., Sharma, J. K., & Khanna, R. (2010). Review of topographic analysis methods for the western Himalaya using AWiFS and MODIS satellite imagery. *Annals of Glaciology, 51*(54), 153–160. https://doi.org/10.3189/172756410791386526

Mohammadi, M., & Sharifi, A. (2021). Evaluation of convolutional neural networks for urban mapping using satellite images. *Journal of the Indian Society of Remote Sensing, 49*. https://doi.org/10.1007/s12524-021-01382-x

Mohammadi, M., Sharifi, A., Hosseingholizadeh, M., & Tariq, A. (2021). Detection of oil pollution using SAR and optical remote sensing imagery: A case study of the Persian

Gulf. *Journal of the Indian Society of Remote Sensing, 49.* https://doi.org/10.1007/s12524-021-01399-2

Moradi, E., & Sharifi, A. (2023). Assessment of forest cover changes using multi-temporal Landsat observation. *Environment, Development and Sustainability, 25*(2), 1351–1360. https://doi.org/10.1007/s10668-021-02097-2

Mountrakis, G., & Heydari, S. S. (2023). Harvesting the Landsat archive for land cover land use classification using deep neural networks: Comparison with traditional classifiers and multi-sensor benefits. *ISPRS Journal of Photogrammetry and Remote Sensing, 200*, 106–119.

Nejad, S. M. M., Abbasi-Moghadam, D., Sharifi, A., Farmonov, N., Amankulova, K., & Laszlz, M. (2023). Multispectral crop yield prediction using 3D-convolutional neural networks and attention convolutional LSTM approaches. *IEEE Journal of Selected Topics in Applied Earth Observations and Remote Sensing, 16*, 254–266. https://doi.org/10.1109/JSTARS.2022.3223423

Panahi, M., Khosravi, K., Golkarian, A., Roostaei, M., Barzegar, R., Omidvar, E., Rezaie, F., Saco, P. M., Sharifi, A., Jun, C., & Bateni, S. M. (2022). A country-wide assessment of Iran's land subsidence susceptibility using satellite-based InSAR and machine learning. *Geocarto International, 37*(26), 14065–14087. https://doi.org/10.1080/10106049.2022.2086631

Panahi, M., Yariyan, P., Rezaie, F., Kim, S. W., Sharifi, A., Alesheikh, A. A., Lee, J., Lee, J., Kim, S., Yoo, J., & Lee, S. (2022). Spatial modeling of radon potential mapping using deep learning algorithms. *Geocarto International, 37*(25), 9560–9582. https://doi.org/10.1080/10106049.2021.2022011

Pande, C. B. (2022). Land use/land cover and change detection mapping in Rahuri watershed area (MS), India using the google earth engine and machine learning approach. *Geocarto International, 37*(26), 13860–13880.

Rasheed, M. U., & Mahmood, S. A. (2023). A framework based on deep neural network (DNN) for land use land cover (LULC) and rice crop classification without using survey data. *Climate Dynamics*, *61*(11), 5629–5652. https://doi.org/10.1007/s00382-023-06874-9

Shao, Y., & Lunetta, R. S. (2012). Comparison of support vector machine, neural network, and CART algorithms for the land-cover classification using limited training data points. *ISPRS Journal of Photogrammetry and Remote Sensing, 70*, 78–87.

Sharifi, A. (2020). Flood mapping using relevance vector machine and SAR data: A case study from Aqqala, Iran. *Journal of the Indian Society of Remote Sensing, 48.* https://doi.org/10.1007/s12524-020-01155-y

Sharifi, A., & Felegari, S. (2022). Nitrogen dioxide (NO2) pollution monitoring with sentinel-5P satellite imagery over during the coronavirus pandemic (case study: Tehran). *Remote Sensing Letters, 13*(10), 1029–1039. https://doi.org/10.1080/2150704X.2022.2120780

Singh, A. (1989). Review article digital change detection techniques using remotely-sensed data. *International Journal of Remote Sensing, 10*(6), 989–1003.

Singh, G., Sethi, G. K., & Singh, S. (2021a). *Performance analysis of deep learning classification for agriculture applications using Sentinel-2 data* (Vol. 1). Springer. https://doi.org/10.1007/978-981-16-3660-8_19

Singh, G., Sethi, G. K., & Singh, S. (2021b). Survey on machine learning and deep learning techniques for agriculture Land. *SN Computer Science, 2*(6), 487. https://doi.org/10.1007/s42979-021-00929-6

Singh, R. K., Singh, P., Drews, M., Kumar, P., Singh, H., Gupta, A. K., Govil, H., Kaur, A., & Kumar, M. (2021c). A machine learning-based classification of LANDSAT images to map land use and land cover of India. *Remote Sensing Applications: Society and Environment, 24*, 100624. https://doi.org/10.1016/j.rsase.2021.100624

Singh, S., Tiwari, R. K., Sood, V., & Gusain, H. S. (2021d). Detection and validation of spatiotemporal snow cover variability in the Himalayas using Ku-band (13.5 GHz) SCATSAT-1 data. *International Journal of Remote Sensing, 42*(3), 805–815. https://doi.org/10.1080/2150704X.2020.1825866

Singh, G., Singh, S., Sethi, G. K., & Sood, V. (2022a). Detection and mapping of agriculture seasonal variations with deep learning–based change detection using Sentinel-2 data. *Arabian Journal of Geosciences, 15*(9), 1–19. https://doi.org/10.1007/s12517-022-10105-6

Singh, G., Singh, S., Sethi, G., & Sood, V. (2022b). Deep learning in the mapping of agricultural land use using sentinel-2 satellite data. *Geographies, 2*(4), 691–700. https://doi.org/10.3390/geographies2040042

Singh, S., Tiwari, R. K., Sood, V., Gusain, H. S., & Prashar, S. (2022c). Image fusion of Ku-Band-based SCATSAT-1 and MODIS data for Cloud-Free change detection over Western Himalayas. *IEEE Transactions on Geoscience and Remote Sensing, 60*. https://doi.org/10.1109/TGRS.2021.3123392

Sood, V., Gusain, H. S., Gupta, S., Singh, S., & Kaur, S. (2020). Evaluation of SCATSAT-1 data for snow cover area mapping over a part of Western Himalayas. *Advances in Space Research, 66*(11), 2556–2567. https://doi.org/10.1016/j.asr.2020.08.017

Taloor, A. K., Kumar, V., Singh, V. K., Singh, A. K., Kale, R. V., Sharma, R., Khajuria, V., Raina, G., Kouser, B., & Chowdhary, N. H. (2020). Land use land cover dynamics using remote sensing and GIS Techniques in Western Doon Valley, Uttarakhand, India. *Geoecology of landscape dynamics* (pp. 37–51). https://doi.org/10.1007/978-981-15-2097-6_23

Tariq, A., Yan, J., Ghaffar, B., Qin, S., Mousa, B. G., Sharifi, A., Huq, M. E., & Aslam, M. (2022). Flash flood susceptibility assessment and zonation by integrating analytic hierarchy process and frequency ratio model with diverse spatial data. *Water (Switzerland), 14*(19). https://doi.org/10.3390/w14193069

Teluguntla, P., Thenkabail, P. S., Oliphant, A., Xiong, J., Gumma, M. K., Congalton, R. G., Yadav, K., & Huete, A. (2018). A 30-m landsat-derived cropland extent product of Australia and China using random forest machine

learning algorithm on Google Earth Engine cloud computing platform. *ISPRS Journal of Photogrammetry and Remote Sensing, 144*, 325–340.

Twisa, S., & Buchroithner, M. F. (2019). Land-use and land-cover (LULC) change detection in Wami River Basin, Tanzania. *Land, 8*(9), 136.

Yao, J., Mitran, T., Kong, X., Lal, R., Chu, Q., & Shaukat, M. (2020). Landuse and land cover identification and disaggregating socio-economic data with convolutional neural network. *Geocarto International, 35*(10), 1109–1123.

Zamani, A., Sharifi, A., Felegari, S., Tariq, A., & Zhao, N. (2022). Agro climatic zoning of saffron culture in Miyaneh City by using WLC method and remote sensing data. *Agriculture (Switzerland), 12*(1), 1–15. https://doi.org/10.3390/agriculture12010118

Zerrouki, N., Harrou, F., Sun, Y., & Hocini, L. (2019). A machine learning-based approach for land cover change detection using remote sensing and radiometric measurements. *IEEE Sensors Journal, 19*(14), 5843–5850.

Zhang, C., Sargent, I., Pan, X., Li, H., Gardiner, A., Hare, J., Atkinson, P. M., Centre, L. E., & La, L. (2019). Remote Sensing of Environment Joint Deep Learning for land cover and land use classification. *Remote Sensing of Environment, 221*(November 2018), 173–187. https://doi.org/10.1016/j.rse.2018.11.014

Zhang, K., Yuan, D., Yang, H., Zhao, J., & Li, N. (2023). Synergy of Sentinel-1 and Sentinel-2 imagery for crop classification based on DC-CNN. *Remote Sensing, 15*(11). https://doi.org/10.3390/rs15112727

Zhang, L., Zhang, L., & Du, B. (2016). Deep learning for remote sensing data: A technical tutorial on the state of the art. *IEEE Geoscience and Remote Sensing Magazine, 4*(2), 22–40. https://doi.org/10.1109/MGRS.2016.2540798

Zhang, Y., Wang, L., Zhou, Q., Tang, F., Zhang, B., Huang, N., & Nath, B. (2022). Continuous Change Detection and Classification—Spectral Trajectory Breakpoint Recognition for Forest Monitoring. *Land, 11*(4), 504.